JOURNAL OF MULTIFUNCTIONAL MATERIALS & PHOTOSCIENCE
8(2), December 2017, pp. 129-156

# Recent Improvements of Graphene Nanocomposites for Dye-sensitized Solar Cells (DSSC) Applications

**Yonrapach Areerob, Won-Chun Oh***

*Department of Advanced Materials Science & Engineering, Hanseo University, Chungnam 356-706, South Korea*

***Abstract:*** The incorporation of graphene-based materials into solar cell represents a cost-effective option to boost its stability, optical transmittance and the overall performance. Graphene has been used as transparent window and counter electrodes, interface layers, hole/electron transport material and also as a buffer layer to slow-down charge recombination in solar cell. Prioritized concern for efficient graphene-based material for dye sensitized solar cell (DSSC) has been motivated by the quest for efficient and low-cost solar cell. In this review, the application of graphene in DSSC was discussed. Promising properties of graphene has shown to enhance various layers of a solar cell. Although layer-by-layer chemical process can detach sections of graphene, this can be improved by doping. Conversion of graphite to graphene enhances the conductivity of photoexcited electrons, electron mobility and reduces the recombination rate of electron/hole pairs. The tunable bandgap properties and excellent thermal and mechanical stability of graphene facilitate the transfer of electrons. RGO improves electron lifetime by increasing the chemical capacitance and decreasing the resistance.

## 1. Introduction

Energy is one the most important problems the world faces today, due to we need energy in every aspect of our daily life [1]. The increasing energy demand of our industrialized civilization is ever hungry for energy and fossil fuel is the only remedy of the time, which already caused the depletion of oil reserves present on the earth crust [2]. At the beginning of the 21$^{st}$ century, the use of fossil fuels notably petroleum, were dominant. Out of the world's total power production, 86.4% is derived from fossil fuels [3]. Unfortunately, each stage in the processing of fossil fuels like extraction, transport, processing, and combustion carry significant and multiple hazards for health and the environment. These impacts include global warming, air quality deterioration, oil spills, and acid rain [4]. These issues recently drive the scientific community to introduce renewable energy resources to meet the increasing energy of human demand and so to protect the world's environment and it living species. This is why, while we have to work to bridge our energy deficit, there is a need to increase the share of clean, sustainable, and renewable energy sources.

*Corresponding author: *wc_oh@hanseo.ac.kr*

Renewable energy which is energy derived from the available sources can be tapped from sun, wind, ocean, hydropower, biomass, geothermal resources, biofuels and hydrogen derived from renewable resources. The sources of these energies are aptly called "renewable" as they can be derived from natural processes which can be constantly replenished within a short time span and not unlike fossil fuels which require millions of years for their formation. Rapid deployment of renewable energy and technological diversification of energy sources would indeed result in significant energy security and economic benefits [6, 7].

Among the renewable energy resources, Photovoltaics (PV) is a technology of generating electrical power by converting solar radiation into direct current electricity using semiconductors. Photovoltaic power generation employs solar panels composed of a number of solar cells containing a photovoltaic material. Solar photovoltaics power generation has long been seen as a clean sustainable energy technology [8]. The direct conversion of sunlight to electricity occurs without any environmental emissions during operation and thus it is eco-friendly.

First in 1991, a dye-sensitized solar cell (DSSC) was proposed and assembled by O'Regan and Grätzel [9]. In recent year DSSCs received global attention due to their several advantages, such as ease of fabrication, can have different color, produce electricity even from stray lights, environmental friendly as compare to other conventional photovoltaic devices [10]. They are based on Nature's principles of photosynthesis. DSSCs are composed of a porous layer of titanium dioxide nanoparticles, covered with a molecular dye that absorbs sunlight very similar to the chlorophyll in green leaves. In addition, It's consists of a photo-electrode and a catalytic-electrode with an electrolyte between them. Photosensitizer absorbs light and injects electrons to the conduction band of the semiconductor. The electrolyte, which is in contact with the dye, then donates electrons to the dye, reinstating it to the initial state. The electrolyte then diffuses towards the counter electrode where the reduction reaction takes place [11,12]. Figure 1 shows basic dye sensitized solar cell architecture.

One of the efficient DSSCs devices uses ruthenium-based molecular dye, e.g. Ruthenium dye (N719), that is anchored to the photoanode via carboxylate ligands. The photoanode consists of 12 ìm thick film of transparent 10–20 nm diameter $TiO_2$ nanoparticles covered with a 4 ìm thick film of much larger (400 nm diameter) particles that scatter photons back into the transparent film. The excited dye rapidly injects an electron into the $TiO_2$ after light absorption. The injected electron diffuses through the sintered particle network to be collected at the front side transparent conducting oxide (TCO) electrode, while the dye is regenerated via reduction by a redox shuttle, $I_3^-/I^-$, dissolved in a solution. Diffusion of the oxidized form of the shuttle to the counter electrode completes the circuit.

The significant collective efforts by the scientific community over the past 20 years have not only pushed the efficiencies higher but have brought out several new ways of making robust and durable DSSC cells fairly affordably with good efficiencies. This has included intense work on various inorganic oxide morphologies, [13-15] sensitizers, [14-

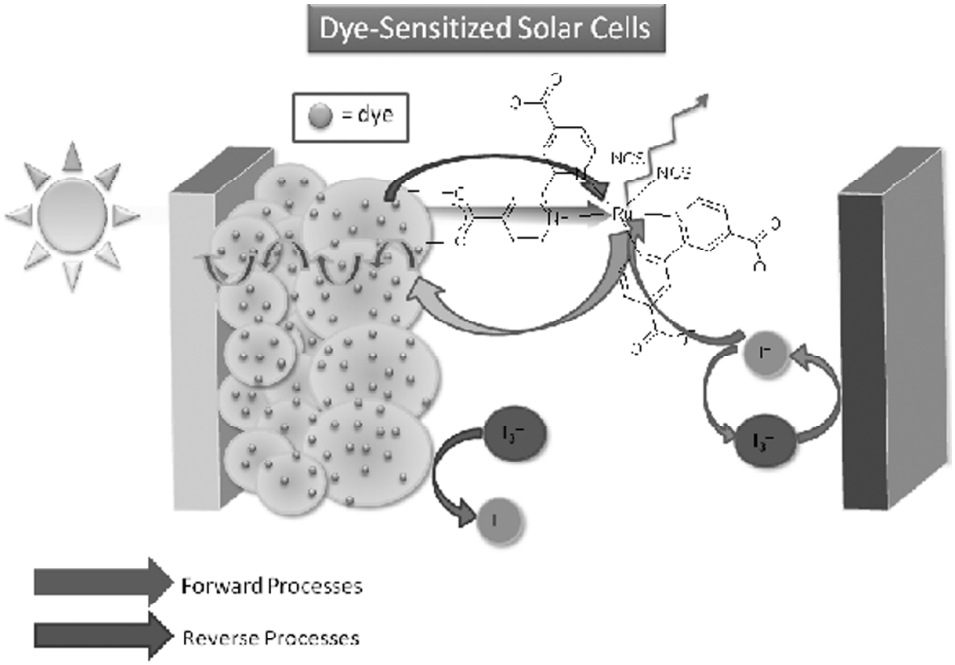


**Figure 1:** Shows basic dye sensitized solar cell architecture. Adapted with permission from ref 2. Copyright 2013 Joseph Roy-Mayhew.

6] co-adsorbers, [17-19] co-sensitization, [20] new counter electrodes, [21] new redox electrolytes [22-25] etc. Till now the best efficiency recorded by these cells is ~13% using co-sensitization of dyes and cobalt redox shuttle as electrolyte. [26] But a major problem of these type of solar cells is the use of liquid electrolyte which evaporates as it contains volatile solvents. Higher temperatures cause the liquid to expand, making sealing of the modules a serious problem. Hence efforts are being made to replace this liquid electrolyte with gel electrolyte or solid hole transporting material (HTM).

## 2. Working DSSC

An efficiency of about 12% has been achieved in DSSCs [27]. The photon incident on the dye, excites the dye. Electrons from excited state of the dye, enters the conduction band of $TiO_2$ (or any semiconductor material used) [28-29]. The electrons then flow through the porous $TiO_2$ thin film to the transparent conducting oxide (TCO). This electron flow depends on the incident intensity and trapping detrapping effect [30]. The oxidized dye molecules are regenerated, when the dye receives electrons from a redox mediator ($I^-/I^-_3$). The mediators are oxidized in the process. Further, these oxidized redox mediators ($I^-_3$) are diffused to the counter electrode where they are regenerated by reduction due to the electrons reaching the counter electrode, through an external circuit, for a complete operation cycle [31]. The working can be understood better from the Schematic band diagram shown in Fig. 2 [32]. The Dye molecule is excited by the incident photon. The excited dye (Dye*) is at a higher energy level and releases an electron into the conduction

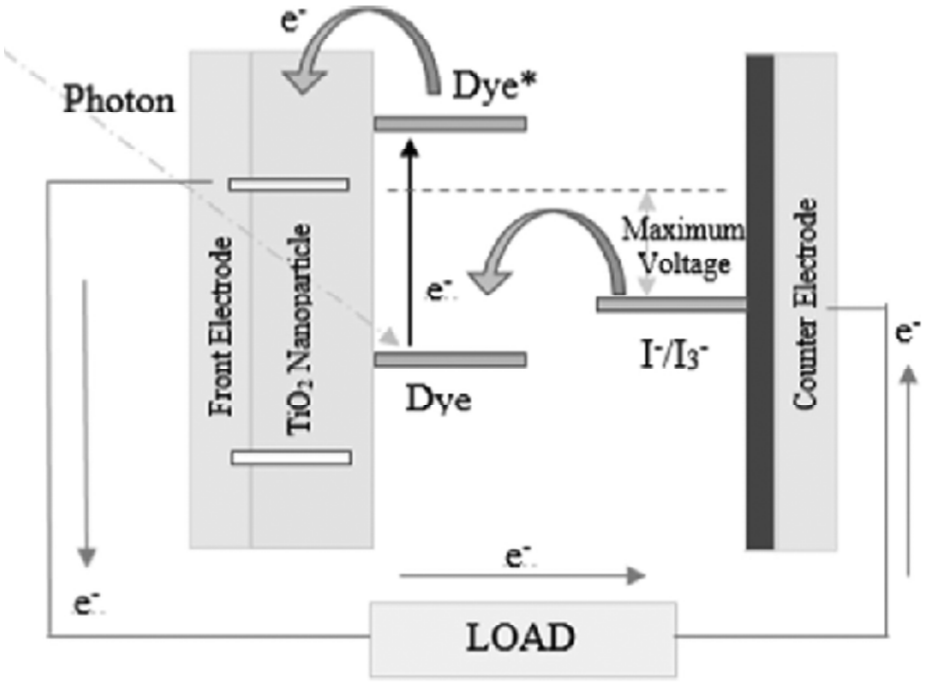


**Figure 2:** DSSC schematic band diagram Copyright 2013 Joseph Roy-Mayhew.

band of the $TiO_2$ (or other nano material like ZnO, CuO, etc.) nano particle, creating a potential difference. This electron is free to move through an external circuit and reach the counter electrode. At the counter electrode and electrolyte interface the electron takes part in the redox reactions and then supplied back to the dye molecules.

All basic components of the DSSC have been worked upon by different researchers, and a number of improvements have been suggested. The improvements have been reviewed and summarized into different categories, as improvements in photoanode, sensitizers, electrolyte and counter electrode.

The overall performance of the solar cell can be evaluated in terms of cell efficiency (ç) and fill factor (FF) expressed as

$$FF = (I_{max} V_{max})/(J_{sc} V_{oc}) \quad (1)$$

$$\eta = ((J_{sc} V_{oc} FF)/P_{in})) \times 100 \quad (2)$$

Where $J_{sc}$ is the short-circuit current density (mA/cm$^2$), $V_{oc}$ the open-circuit voltage (V) and Pin the incident light power. $J_{max}$ and $V_{max}$ correspond to current and voltage values, respectively; at which the maximum power output is derivable as shown in Fig 3.

### *2.1. Short Circuit Current ($J_{SC}$)*

It is the current obtained from the cell when it is short circuited or in other words when the load resistance is zero. It largely depends on the photon generated electrons and the

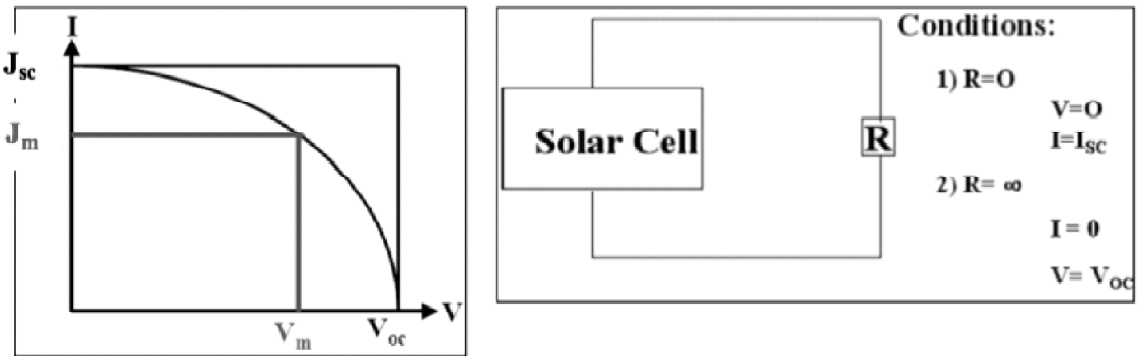


**Figure 3:** Important parameters of Solar cell Copyright 2010 American Chemical Society.

interfacial recombination of the electrons and holes. Solar cell current is normally represented as current density, $J_{sc}$, $J_{sc} = I_{sc}/A$ (mA/cm$^2$), Where, $A$ is the effective area of the solar cell. It is a function of the solar illumination, optical properties and charge transfer probability of the cell.

### *2.2. Open-Circuit Voltage (VOC)*

Open-circuit voltage is the maximum voltage obtainable from a solar cell and is obtained when a load with infinite resistance is attached to its terminals. It is determined by the difference between the redox potential of the electrolyte and Fermi level of electrons in the semiconductor namely $TiO_2$. For DSC the Voc is given by:

$$Voc = ECB/q + kT/q \ln(n/NCB) - E_{redox}/q \text{ (volts)}$$

where, n is the number of electrons in the $TiO_2$ conduction band and NCB is the effective density of states. The first two terms define the quasi-fermi level of $TiO_2$ and Eredox is the Nernst potential of the redox mediator.

### *2.3. Series Resistance (Rs)*

Series resistance, $R_S$ in a solar cell, is the result of the contact resistance and charge transfer resistance in the semiconductor material. Series resistance reduces the fill factor of the device and thus affects the maximum device power output, while excessively high value of RS can also reduce the short-circuit current. The open-circuit voltage is not affected by Rs, since at $V_{oc}$ the total current flow through cell itself is zero and hence through the series resistance is zero. An approximate value of the series resistance can be determined from the slope of the I-V curve at the open-circuit voltage point.

### *2.4. Shunt Resistance (Rsh)*

Low shunt resistance provides an alternate current path for the photo-generated current causing significant power loss. Low shunt resistance reduces the fill factor and lowers the open-circuit voltage, thereby affecting the maximum power output. The short-circuit

current is not affected by shunt resistance unless for its very low value, since at $J_{SC}$ the total current flows through the outer path and hence through the shunt resistance is low. An approximate value of the shunt resistance can be obtained from the slope of the I-V curve at the short circuit current point.

### *2.5. Fill Factor (FF)*

The fill factor (FF) is a measure of the maximum power output from a solar cell. It represents the squareness of the I-V curve and is defined as the ratio of the maximum power to the product of $V_{OC}$ and JSC for the solar cell:

$$FF = Vm * Jm / Voc * Jsc$$

where, Vm and Jm are the voltage and current values at maximum power point. Fill factor, being a ratio of the same physical parameters, has no unit. Fill factor is a function of the series and shunt resistances of the solar cell. For DSSC, it reflects the extent of electrical and electrochemical losses during cell operation. To obtain higher fill factor improvement of the shunt resistance and decrement of the series resistance are required.

### *2.6. Power Conversion Efficiency*

The power conversion efficiency of a solar cell is defined as the ratio of the maximum electrical energy output to the energy input from the sun. Thus the mathematical definition of efficiency is,

$$\eta = (Voc * Isc * FF) / Pin$$

where, Pin is the power input from the sunlight. Efficiency is generally expressed in percentage. Besides the solar cell performance itself, it depends on the incident light spectrum and intensity as well as operating temperature. The internationally recognized standard condition for the efficiency measurement of solar cells is under 'AM1.5 Global' solar irradiation and at a temperature of 25°C.

## 3. Graphene and Dye-sensitized Solar Cells

### *3.1. Graphene*

New materials play an important role in developing solar energy technologies. Graphene, one of the allotropes of abundantly available carbon, has emerged as one of the most promising materials for applications in solar cells since its discovery in 2004 after Novoselov *et al.* [33] reported an electric field effect in a few-atoms-thick layer of graphene. Geim and Konstantin of the University of Manchester received the 2010 Nobel Prize in Physics for their pioneering research on graphene. Graphene is a 1-atom-thick transparent layer of $sp^2$ -hybridized carbon atoms packed into a 2D nanostructure. Room temperature carrier mobilities of 10,000 $cm^2/Vs$ have been reported for few-layer graphene (FLG). [34] Nair *et al.* [35] measured 97.7% optical transparency for a single layer of graphene that decreases as the number of graphene layers increase, and where each additional graphene layer adds 2.3% opacity. Therefore, both optical transparency and the resistance of graphene

decrease with an increasing number of graphene layers. High carrier mobility, low sheet resistance, and high optical transparency are important criteria when considering a material for solar cell applica- tions; graphene fits perfectly as a transparent conductive electrode (TCE) material. Lee *et al.* [35] reported a Young's modulus of 1.02 terapascals (TPa) for bulk graphite, establishing graphene as the strongest material. Zhang *et al.* [36] demonstrated by thermogravimetric analysis (TGA) that the initial reduction of graphene oxide (GO) occurs at 100 °C with the removal of absorbed water molecules, and thereafter a 30% weight loss in 110–230 °C takes place due to the decomposition and removal of thermal- liable oxygen functional groups from the GO surface. Shen et al. [37] conducted a TGA of reduced graphene oxide (rGO) and indicated that the removal of oxygen functional groups increases thermal stability for rGO, which has only 2% weight loss at 700 °C in a nitrogen atmosphere. As discussed above, graphene shows unique electrical, mechanical, thermal, chemical, and optical properties due to its 2D characteristics, which can be further tailored via processing into different forms. The 2D graphene structure can be transformed into large-area stretchable ultra- thin films, nanoribbons, foams, [38, 39] and large-area graphene paper [40] and sheets. [41] Pristine graphene has no bandgap; therefore, it acts as a semimetal. Scientists are exploring new chemical and physical ways to create an artificial bandgap in graphene, which is one of the require- ments for the fabrication of electronic devices. Zero- bandgap graphene can be transformed into a wide-bandgap semiconductor through hydrogenation via $sp^3$ C–H bond formation. [42] Balog *et al.* [43] reported a bandgap opening in graphene by the patterned adsorption of atomic hydrogen onto the Moireì superlattice positions of graphene when graphene grown on an Ir (111) substrate was exposed to a dose of atomic hydrogen. Fully or partially hydrogenated graphene exhibits different structural, thermopower, electronic, magnetic, and transport properties from pristine graphene. [44-45] Because graphene is an atom-thick layer, it is a perfect nanoscale material and, therefore, has great potential in a very wide range of applications in the fieldof nanotechnology. Nanoscale carbon materials such as fullerenes, CNTs, diamonds, amorphous carbon, and theircomposites have been widely studied for nanotechno-logical applications, [46-50] including nanoelectronics, nano-optics, display devices, LEDs, computer data storage, energy, membranes, nanofilters for water purification, sensors, nanomedicine, stem cells, and energy conversion devices. The emergence of nanotechnology has significantly impacted high-tech industries and research where metal and metal oxide nanoparticles, nanotubes, nanowires, and quantum dots can now replace conventional semiconductor materials in solar cell devices. Graphene is a 2D carbon-based material having a single layer of carbon atoms; therefore, it is a simple nanostructured material. Because of this, graphene has been extensively studied for nanotechnological applications in field-effect transistors, solar cells, fuel cells, supercapacitors, rechargeable batteries, optical modulators, chemical sensors, drug delivery, and biomedical applications, in addition to other areas. [51-53].

Graphite oxide or graphene oxide (GO) contains hydroxyl (–OH) and epoxide (–C–O–C–) functional groups on the basal planes, and carbonyl (–COH) and carboxyl (–COOH) functional groups at the edges. [54-56] Gao *et al.* reported the presence of 5- and 6-membered-ring lactols in a graphite oxide structure. [57] Therefore, graphite oxide has a

heterogeneous electronic structure due to its mixed $sp^2$ and $sp^3$ hybridizations. [58-60] These functional groups can be partially removed either by thermal annealing or by chemical treatment from graphite oxide, [61-65] however, a few of these oxygen groups are still retained in graphene sheets. A systematic study on the reduction of GO was conducted by Mathkar *et al.* [65] to tailor the bandgap. By a controlled reduction process, the optical bandgap of GO was found to change from 3.5 eV to 1.0 eV. The structural changes from GO to rGO and then to graphene are accompanied by gradual changes in optical bandgap, electrical conductivity, carrier mobility, and thermal stability. These parameters significantly affect the pho- tovoltaic properties and stability of graphene-based solar cells. GO is hydrophilic in nature, while graphene attains a hydrophobic characteristic after a complete removal of all oxygen functional groups from the GO surface. Oxygen functional groups on the GO surface offer tremendous possibilities for chemical functionalization of the GO surface, from small molecules to macrocyclic structures, to be used in drug delivery, electronics, solar cells, and other applications. GO, rGO, and graphene have been extensively studied for both DSSC devices as well as bulk-heterojunction solar cells. This review focuses solely on applications of graphene-based materials in fabricating DSSC devices.

## 4. The detailed structure of DSSC

The dye sensitized solar cell consists of five main components: transparent conductive oxide (TCO) coated substrate, metal oxide coating, dye, electrolyte and counter electrode material.

### *4.1. The TCO glass substrate*

The transparent conducting substrate plays an important role in dictating the DSSC's performance. It functions as a current collector and a support of the semiconductor layer in DSSC. It has two important features: the high optical transparency which allows natural sunlight to pass through to the beneath of the active material without unwanted absorption of the solar spectrum, and low electrical resistivity which facilitates the electron transfer process and reduces the energy loss. Current transparent conducting oxides used in industry are primarily n-type conductors.

Transparent conducting coatings for photovoltaic applications have been fabricated using both inorganic and organic materials. Inorganic films typically are made up of a layer of transparent conducting oxide (TCO), [66] generally in the form of indium tin oxide (ITO), fluorine doped tin oxide (FTO), and doped zinc oxide. Organic films are being developed using carbon nanotube networks and graphene, which can be fabricated to be highly transparent to infrared light, along with networks of polymers such as poly(3,4-ethylenedioxythiophene) and their derivatives. The most efficient TCO material widely used in photovoltaic application is ITO or FTO coated glass substrate. However, the only concern with ITO is that its conductivity decreases during the calcinations process in the DSSCs fabrication. Therefore, FTO is the preferred transparent conducting material for DSSCs. TCO films are deposited on a substrate through various deposition methods,

including metal organic chemical vapour deposition (MOCVD), spray pyrolysis, and pulsed laser deposition (PLD), however the most efficient technique is magnetron sputtering of the film.

### *4.2. Metal Oxide Coating*

The metal oxide nanoparticulate porous coating is generally deposited on the top of the TCO by doctor blade method or screen printing method. This coating provides a surface for the dye adsorption, it accepts electrons from the excited dye, and conducts electrons to the TCO. The choice of metal oxide can be made between different n-type oxides such as $TiO_2$, ZnO, [67] $SnO_2$ [68] and other ternary oxide like $Zn_2SnO_4$ [69] etc. $TiO_2$ is the work horse material for DSSCs. It exists in three forms namely anatase, rutile and brookite. Of the three forms rutile is the most stable phase but it suffers from slow electron transfer rate leading to low current in DSSC. Anatase $TiO_2$ is widely used as a photo-anode material which renders conversion efficiency of 12% due to greater electron transport properties and high surface area. Zinc oxide (ZnO) is a promising alternative to $TiO_2$ because it has a similar band structure and relatively high electron mobility (1–5 $cm^2 V^{-1} s^{-1}$). [70] However it is not stable in the most efficient dyes containing acidic groups which are required for anchoring of the dye on the metal oxide surface. Alternatively, tin oxide ($SnO_2$) is an attractive option but it shows poor photovoltaic performance due to faster recombination dynamics and lower isoelectric point leading to poor dye loading on its surface. [71] Thus in this thesis work $TiO_2$ nanoparticle films are used as the working electrode.

### *4.3. The Sensitizer*

The ideal sensitizer used in DSSC has to meet several requirements that guide effective molecular engineering : (i) the sensitizer should be able to absorb all incident light below the near-IR wavelength of approximately 920 nm; (ii) it must carry a carboxylate or phosphonate group to anchor on the surface of the semiconductor oxide; (iii) the lowest unoccupied molecular orbital (LUMO) of the sensitizer must match the edge of the conduction band of the oxide to minimize the energetic potential losses during the electron transfer reaction; (iv) the highest occupied orbital (HOMO) of the sensitizer must be sufficiently low to accept electron donation from an electrolyte or a hole conductive material; (v) it should be stable.

The sensitizer, or dye monolayer, is the layer which interacts with the sunlight and therefore is a very important part of the DSSC. Typically, the metal oxide films are immersed in the dye solution for 12 to 24 h so that the dye molecules get adsorbed on the surface of the metal oxide nanoparticles. Ruthenizer 535-bisTBA (also known as N719) and Ruthenizer 535 (also known as N3 dye) (Figure 4) in the literature, have been so far the most efficient sensitizers in Dye Solar Cells which sensitize wide band-gap oxide semiconductors, like titanium dioxide, very efficiently up to a wavelength of 750 nm. The photovoltaic performance of black dye is expected to be superior to all other known charge-transfer sensitizers in terms of the whole range of light absorption. But the high cost, the limited abundance and availability of noble metals, and also the sophisticated synthesis and

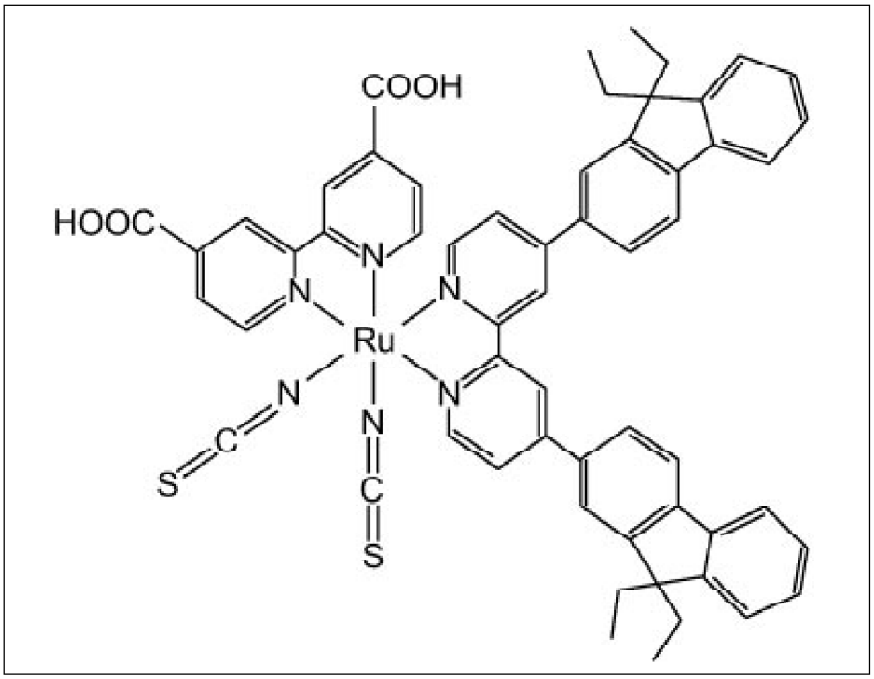


**Figure 4:** Ruthenium dyes

purification steps have pushed the scientific community to search for some metal free organic dyes and even natural dyes as well.

### *4.4. The Electrolyte*

The electrolyte is a key component of dye-sensitized solar cells (DSSCs). It functions as charge carrier collecting electrons at the cathode and transporting the electrons back to the dye molecule. The most commonly used liquid electrolyte, namely iodide/ triiodide ($I^-/I_3^-$), works well mainly due to its kinetics. Figure 5 shows the kinetics of $I^-/I_3^-$ redox couple with Ru-N719 dye. The electron injection into the $TiO_2$ conduction band occurs in the femto second time scale which is much faster than the electron recombination with $I_3^-$, and the oxidized dye preferably reacts with I- than combining with the injected electrons. In the electrolyte, the $I_3^-$diffuses to cathode to harvest electrons and in turn produce $I^-$ which diffuses in the opposite direction towards the $TiO_2$ electrode to regenerate the dye molecules. The diffusion coefficient of $I_3^-$ ions in the porous $TiO_2$ structure is about 7.6 $x10^6$ $cm^2/s$. [72] It is found that recombination can be suppressed by introducing additives to the electrolyte such as 4-tert-butylpyridine (4TBP) [73], guanidiumthiocyanate [74], and methylbenzimidazole (MBI) [75]. The most probable mechanism is that these additives, when absorbed by the$TiO_2$ surface, block the reduction sites to keep electron acceptor molecules away from contact.

The overall conductivity of this electrolyte can also be increased by using different ionic liquids containing imidazolium salts. [76] Depending on the alkyl chains attached

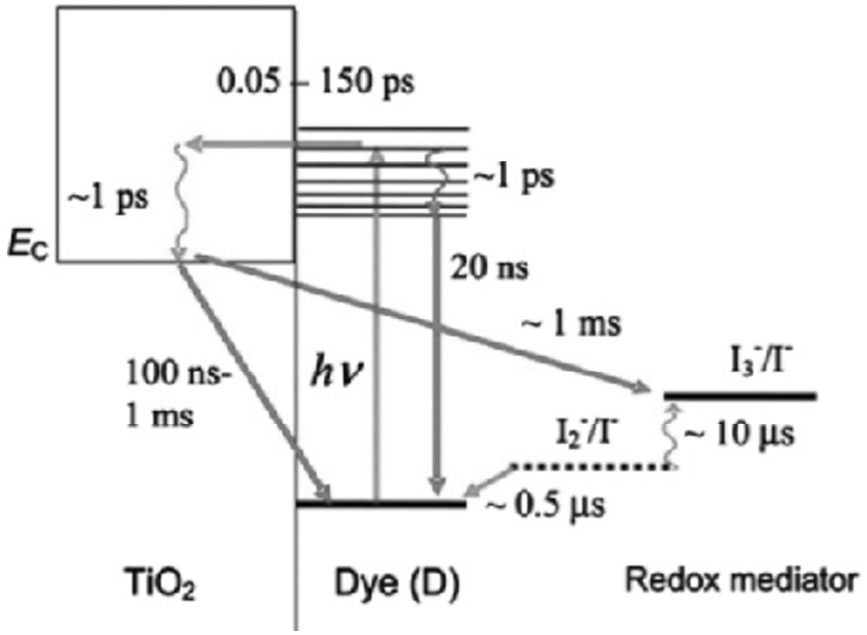


**Figure 5:** Kinetics of the cis- $Ru(dcbpy)_2(NCS)_2$- (N719) sensitized $TiO_2$ solar cell with $I^-/I_3^-$ redox mediator. Copyright 2005 American Chemical Society.

to these imidazolium salts the performance of the electrolyte can be varied. These additives can thus improve the efficiency and stability, though they do not participate in the fundamental photo-electrochemical processes. Lithium iodide is added in the electrolyte as it acts as a source of iodide ions required for redox couple in electrolyte. Also the Lithium ions screen the negative charge in the semiconductor, and increases charge conductivity in the electrolyte. [77] In absence of these cations on the surface the conduction band of semiconductor shows a downward shift which gives lowers the Voc of the cell. [78] But the concentration of this LiI must not be very high as the small Li cations can intercalate with the $TiO_2$ matrix and act as recombination centers thus lowering the device performance. In theory, the maximum voltage generated in DSSCs is determined by the difference between the quasi-Fermi level of the $TiO_2$ and the redox potential of the electrolyte, about 0.7 to 0.8 V under solar illumination conditions. In order to obtain a higher open circuit voltage and control the corrosion of $I^-/I_3^-$ redox couple, a variety of alternative redox couples have been introduced in DSSCs such as $Br^-/Br_3^-$, $SCN^-/(SCN)_2$, $SeCN^-/(SeCN)_3^-$, $Fe(CN_{)6}$ 3-/4- 47 and Co(II)/Co(III)complex. In this thesis work liquid $I^-/I_3^-$ redox electrolyte with suitable additives is used as the electrolyte. The composition details are described in the next chapter.

### *4.5. The Counter electrode*

Usually Pt nanoparticle-coated FTO obtained by thermal decomposition, [79] sputtering [80] or chemical reduction [81] is used as the counter electrode. Pt counter electrode is

very efficient in $I^-/I_3^-$ redox regeneration (the conversion of $I_3^-$ to $I^-$ occurs on the surface Pt) which in turn helps in the regeneration of oxidized dye. Thus, platinum acts as catalyst for the charge transfer reaction occurring between iodide and tri-iodide. [82] However in view of the high cost and less natural abundance of Pt, in recent years significant efforts are directed towards the replacement of this Pt catalyst with other inexpensive and earth abundant materials. [83]

The pre-requisites for an efficient catalyst in DSSC are that it should be easily available, low cost, stable in the cell architecture ambient and certainly with a very good catalytic activity. Carbon is one of the leading candidates in this respect. Till today various carbon forms like CNTs, [84] functionalized graphene, [85] mesoporous carbon, [86] carbon fibers, [87] laser synthesized carbon [88] etc. have been successfully used as counter electrodes in DSSCs with efficiency comparable to or even exceeding that of platinum. But the main problem of carbon counter electrodes is adhesion of these carbon materials to the substrate surface and its opaque nature. Inorganic materials like sulphides, carbides, nitrides and some organic/inorganic composites can also be used as the counter electrode materials. [89] In this thesis work drop casted and thermally deposited Pt is used as counter electrode.

## 5. Graphene based Counter electrode for Dye-sensitized Solar Cells

### *5.1. Graphene Materials for CEs*

The first study incorporating graphene materials as the catalytic cathode of a DSSC that we are aware of was by Xu *et al.,* where pyrenebutyrate was used to stabilize chemically reduced graphene oxide (CRGO) suspensions for processing into a film. [90] Although the film worked better as a cathode in a DSSC ($\eta = 2.2\%$) than bare FTO did ($\eta = 0.05\%$), it was obvious that many improvements would have to be made to be able to compete with the conventional platinized FTO ($\eta = 4.0\%$). Choi *et al.* found similar performance limitations using graphene oxide films which had undergone mild thermal treatment (250 °C, 2 min in air) [91] Hasin et al. compared TRGO and CRGO films and found that the former exhibit about one-fourth of the $R_{CT}$ of the latter.200 Nevertheless, this resistance was still over 70 times greater than that of platinized FTO ($R_{CT} \approx 180$, 48, and 0.66 $\Omega$ cm$^2$ for CRGO, TRGO, and platinized FTO electrodes). Although not focused on in their work, this result could be indicative that defect sites created through thermal reduction could be catalytic for the triiodide reduction. Roy-Mayhew *et al.* looked to improve upon these results by utilizing a porous network of TRGO formed through spin coating a polymer–TRGO composite and thermalizing the polymer binder. [92] This work showed that TRGO films could be a viable competitor for platinum (TRGO $R_{CT} = 9.4\ \Omega$ cm$^2$, $\eta = 5.0\%$; platinized FTO $R_{CT} = 1.3\ \Omega$ cm$^2$, $\eta = 5.5\%$) and suggested that the functional groups and defects could play an important role in catalysis. Since then a series of studies has been published analyzing how the degree of reduction affects catalytic perform- ance. [93-99] Zhang *et al.* found that thermal annealing of porous CRGO films increased activity up to 400 °C in air, above which activity decreased. [100] The reported $R_{CT}$ for the T-CRGO film at 400 °C was ~ 280 times lower than that for electrodes heated only to 250 °C the lowest used in the study and similar to the treatment reported for Choi *et al.* above. Unlike the T-CRGO

films used by Zhang *et al.*, a separate study by Choi *et al.* showed a monotonic decrease in RCT for CRGO thermally treated at progressively higher temperatures up to 600 °C, the maximum used in their study. [101] Hsieh *et al.* also report a monotonic increase in performance with an increase in reduction temperature of graphene oxide, with films (20 ìm thick with 5% polyvinylidene fluorine, PVDF) annealed at 700 °C exhibiting an RCT of 22 Ω $cm^2$. [102] Nevertheless, device efficiency was only slightly over one-half that of cells using sputtered platinum. Jang *et al.* report an increase in activity upon thermal treatment of 200 nm thick electrosprayed CRGO films and believe it is due to an increase in network conductivity (by a factor of ~ 40) rather than to the intrinsic activity of the material. [103] They follow this work up with a systematic study of thermal annealing of flat films of graphene oxide (~ 4 nm thick). [104] Morphology is minimized in this system, so the changes seen are due to the material rather than the structure. Detailed electrochemical studies were not undertaken; nevertheless, the authors show a strong increase in performance with increased temperature treatment (η = 0.50%, 0.51%, 2.9%, and 3.6% for graphene oxide and graphene oxide thermally reduced at 150, 250, and 350 °C, respectively). Although impressive improvement was seen, the best cells only exhibit a fill factor of 0.33 and are significantly worse than the platinized FTO electrode (n = 6.4%), reinforcing the relative inertness of the carbon material for the iodide-based redox mediator.

As introduced above, two main approaches to overcome the limitation of a relatively inert material have been taken: (i) improving morphology, generally by increasing the surface area and pore size, [105-110] and (ii) increasing the intrinsic activity of the material through chemical modification. [111] With the first approach, a straightforward technique is to use more material and make a thicker film; however, simple liquid- processing techniques such as vacuum filtration do not produce films which can compete with platinum. [106] Wu and Zheng created horizontal oriented CRGO using spin coating and vertically oriented CRGO using electrophoretic deposition. [107] In their system they showed that the vertical orientation had greater activity, suggesting that ion mobility and assessable surface area was higher in this system. However, the deposition procedure used $NiCl_2$, so we cannot rule out that the improved performance was due to the 1 wt % of Ni that was deposited during the process. In another study, Zheng *et al.* showed that grinding CRGO in poly(ethylene glycol) and then thermolyzing the polymer led to films with larger pores (by ~ 1 nm) and DSSCs with higher efficiencies (η = 7.2%) than those created from ultrasonicating CRGO in the polymer (η = 5.2%). Even so, these devices still did not match the performance of those using platinized FTO (η = 7.8%). To create high surface area electrodes, Lee *et al.* first created a $NiCl_2$–poly(vinyl alcohol) film and then pyrolyzed it to form a porous nickel substrate. [108] Through CVD processing and subsequent etching of the metal scaffold, a porous (average pore size 40-50 nm) CVD-derived graphene structure was formed. Another approach was to use spacers to keep RGO sheets apart and thus increase the surface area. Gong et al. used 12 nm $SiO_2$ particles as spacers to increase their CRGO film specific surface area from 8.6 to 383.4 $m^2/g$. [109] Even with the improvement, platinized FTO performed 6% better, relatively, than the film with spacers. Roy- Mayhew *et al.* were able to match the performance of platinized FTO (η = 6.8% for both) by doctor blading a TRGO (Vor-x, Vorbeck Materials Corp.) film

with an ethyl cellulose binder and then partially thermalizing the binder, leaving behind an insoluble residue that prevented TRGO sheets from restacking. [110]

Rather than focusing on increasing the surface area, several groups worked on increasing the intrinsic activity of the material through chemically doping the material. Yen *et al.* over doubled the efficiency of their CRGO–PVDF–[carbon black] films (from $\eta$ = 1.9% to $\eta$ = 4.8%) by incorporating nitrogen into them through hydrazine reduction in the presence of ammonia. [111] Similarly, Xue *et al.* created nitrogen-doped graphene through annealing graphene oxide in an argon and ammonia atmosphere, and this material outperformed traditional TRGO in a DSSC, reportedly due to an increase both in catalytic structural defect density and in conductivity. [112] Nevertheless, in the same study, better performance was seen with high surface area nitrogen-doped graphene created through annealing freeze-dried graphene oxide. Images of these electrodes are shown in Figure 6 and 20C. They formed counter electrodes from this material by mixing it with poly(ethylene oxide), coating FTO, and thermalizing the binder. The authors report lower RCT than platinum with these films; however, in contradiction to these results, DSSCs using platinized FTO were reported to have slightly higher efficiencies ($\eta$ = 7.4% compared to $\eta$ = 7.1%). As mentioned previously, where there is a discrepancy between EIS or CV results and $\eta$, such as that just described; the results are highlighted in bold font.

## 6. Nanomaterials Characterization techniques

### *6.1. X-Ray Diffraction*

X-ray diffraction (XRD) technique is used to realize structural properties of materials and get information like crystal structure/phase, lattice parameters, crystallite size, orientation of single crystals, preferred orientation of polycrystals, defects, strains and so on. [113] This technique is suitable for thin films, bulk and nanomaterials. In the case of nanostructures, the change in lattice parameter w. r. t. bulk gives an idea of nature of strain present in the film. In XRD, a collimated monochromatic beam of X-rays is incident on the sample for diffraction to occur. A constructive interference occurs only for certain è's correlating to those (hkl) planes, where path difference is an integral multiple (n) of wavelength. Based on this, the Bragg's condition is given by

$$2d\sin\theta = n\lambda \quad (4)$$

Where, $\lambda$ is the wavelength of the incident X-ray, d is the inter-planer distance, '$\theta$' is the scattering angle and n is an integer-called order of diffraction. In nanostructures, X-rays are diffracted by the oriented crystallites at a particular angle to satisfy the Bragg's condition. Having known the value of $\theta$ and $\lambda$, one can calculate the inter-planer spacing. The XRD can be taken in various modes such as $\theta$ - 2$\theta$ scan mode, $\theta$ - 2$\theta$ rocking curve, and $\varphi$ scan. In the $\theta$ - 2$\theta$ scan mode, a monochromatic beam of X-rays is incident on the sample at an angle of $\theta$ with the sample surface. The detector motion is coupled with the X-ray source in such a way that it always makes an angle 2$\theta$ with the incident direction of the X-ray beam (Figure 7). The resulting spectrum is a plot between the intensity recorded by the detector versus 2$\theta$.

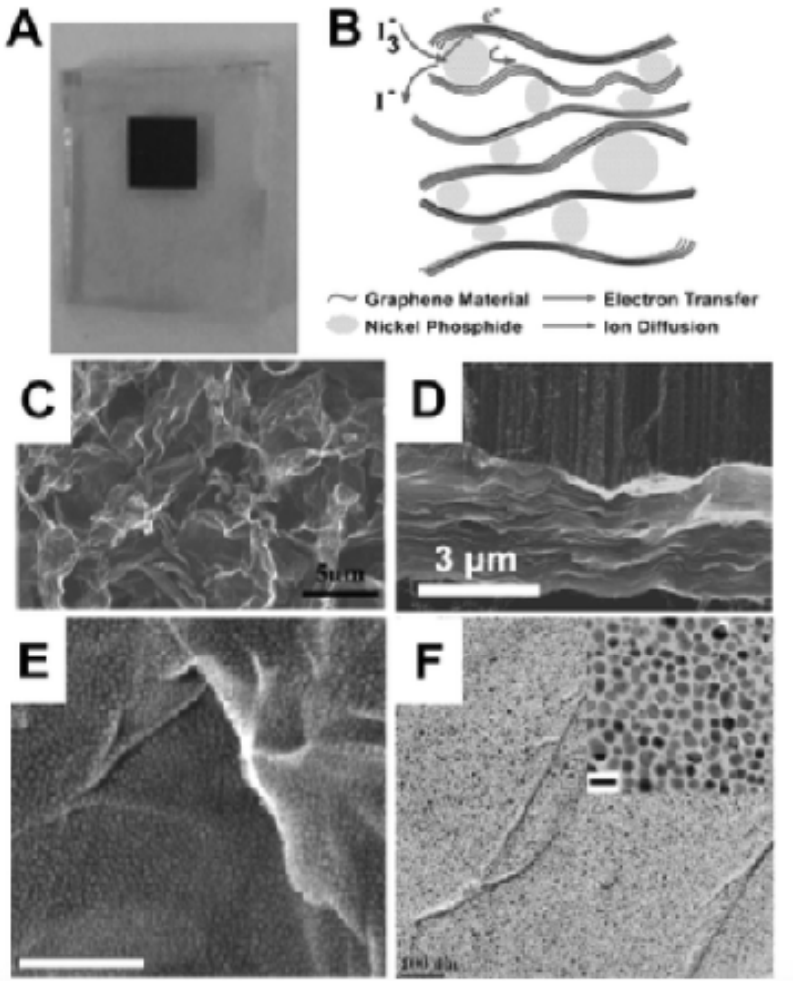


**Figure 6:** Graphene material electrodes for catalysis. (A) Optical image of a typical opaque graphene material electrode. Adapted with permission from ref 211. Copyright 2012 John Wiley & Sons. (B) Schematic of the use of graphene materials as conductive scaffolds for high-activity materials. Similar depiction to that in Dou *et al.* 194 (C) SEM image of porous nitrogen-doped graphene film, as shown in A. Adapted with permission from ref 211. Copyright 2012 John Wiley & Sons. (D) SEM image of CNT-TRGO hybrid electrode wherein TRGO acts as a conductive base for vertically aligned CNTs. Adapted with permission from ref 214. Copyright 2011 John Wiley & Sons. (E) SEM image and (F) TEM image of nickel nanoparticles deposited on TRGO. Scale bar for E is 100 nm. Inset scale bar for F is 10 nm. Adapted with permission from ref 112. Copyright 2011 American Chemical Society.

$$\text{Angle of Incidence } (\theta i) = \text{Angle of Reflectance } (\theta r) \quad (2)$$

This is done by moving the detector twice as fast in (θ) as the source. So, only where θi = θr, will be the intensity of the reflected X-rays to be measured. Nanomaterials have smaller sized crystallites and significant strains due to surface effects, causing considerable peak broadening and shifts in the peak positions w.r.t standard data.

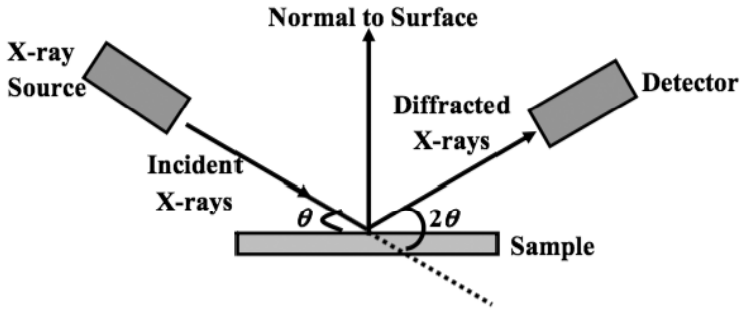


**Figure 7:** Representation of X-ray Diffraction. Copyright 2013 Joseph Roy-Mayhew.

The θ-2θ scan maintains these angles with the sample, detector and X-ray source. Only planes of atoms that share this normal will be seen in the θ-2θ scan. From the shifts in the peak positions, one can calculate the change in the d-spacing, which is the result of change of lattice constants under strain. The crystallite size (D) is calculated using Scherrer's formula:

$$D = k\,\lambda \,/\, \beta \cos\theta \tag{3}$$

Where, $k$ = Scherrer's Constant ≈ 0.9, β = Full Width at Half Maximum (FWHM). The only disadvantage of XRD is its less sensitivity towards low-Z materials, thus usually high-Z materials can be better characterized. In such cases, electron or neutron diffraction is employed to overcome the low intensity of diffracted X-rays [114].

### *6.2. Transmission Electron Microscopy (TEM)*

Transmission electron microscopy (TEM) is an imaging technique whereby a beam of electrons is focused onto a specimen causing an enlarged version to appear on a fluorescent screen or a layer of photographic film, or to be detected by a CCD camera. TEM operates on the same basic principles as the light microscope but uses electrons instead of light. The line diagram of a typical TEM column is shown in Figure 8. The column consists of a source of electrons, electrodes for electron acceleration, electromagnetic focusing and deflecting lenses and the electron detection system such as a CCD array. By using electron energy of several hundred kilovolts the de Broglie wavelength associated with the electron can be reduced to a small fraction of nanometer and hence atomic resolution imaging becomes feasible. Virtually, TEM is useful for determining size, shape and arrangement of the particles which make up the specimen. Moreover, it is highly useful for the determination of the lattice planes and the detection of atomic-scale defects localized in areas of few nanometers in diameter with the help of selected area electron diffraction (SAED) technique. The d- spacing between lattice planes of crystalline materials can be calculated from a SAED pattern using the relationship:

$$dr = \lambda L \tag{4}$$

where, L is the distance between the specimen and the photographic plate, λL is known as the camera constant and r is the radius of diffracted rings. It is easy to measure r directly

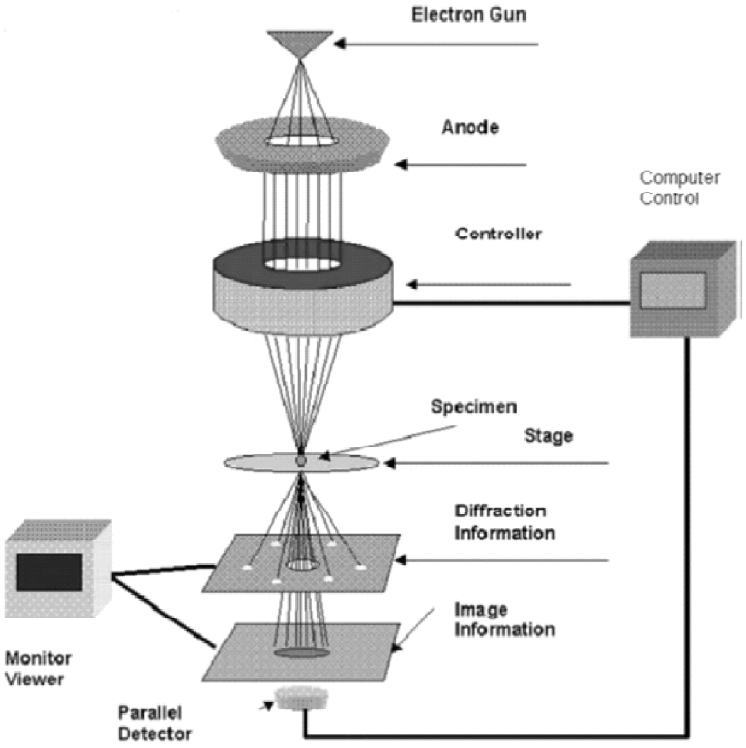


**Figure 8:** Schematic diagram of the Transmission Electron Microscope. Copyright 2013 Joseph Roy-Mayhew.

from the photographic plate, and λL can be established from the instrument by calibrating it with a standard material (usually Ag), and hence one can easily get d values. Since, each d value corresponds to a specific lattice plane for a specific crystal structure; description of the crystal structure of a crystalline specimen can be obtained from SAED pattern. In some cases SAED pattern is more helpful as compared to XRD, due to the limited detection limit of XRD instrument. Also, the XRD generally gives global information [115].

The TEM measurements in the present work were performed on a JEOL JEM-1200EX instrument operating at 300 kV, camera length of 80 cm and field limited aperture of 100 ìm. Prior to TEM measurements, the samples were dispersed in a suitable organic solvent (isoamyl acetate, methanol, acetone, toluene, etc.) and a drop of the solution was poured on carbon-coated copper grid of 400 mesh size. The film formed on the TEM grids was allowed to dry for 2 minutes following which the extra solvent was removed using a blotting paper and the TEM and SAED measurements were performed. The image and diffraction analysis were performed under an accelerating voltage of 300 kV. Experimental electron diffraction patterns of various samples were compared with the simulated electron diffraction patterns of the corresponding phases. Electron diffraction ring patterns were simulated using the computer program JECP/PCED.

### *6.3. Scanning Electron Microscope (SEM)*

It uses a beam of electrons focused to a diameter spot of approximately 1nm in diameter on the surface of the specimen and scanned back and forth across the surface (beam energy of 200kV). The surface topography of a specimen is revealed either by the reflected (backscattered) electrons generated or by electrons ejected from the specimen as the incident electrons decelerate secondary electrons. A visual image, corresponding to the signal produced by the interaction between the beam spot and the specimen at each point along each scan line, is simultaneously built up on the face of a cathode ray tube similar to the manner by which a television picture is generated. The best spatial resolution currently achieved is of the order of 1nm.

The scanning electron microscope (SEM) is a very useful instrument to get information about topography, morphology and composition information of materials. A typical schematic of a SEM is shown in Figure 9. It is a type of electron microscope capable of producing high resolution images of a sample surface. Due to the manner in which the

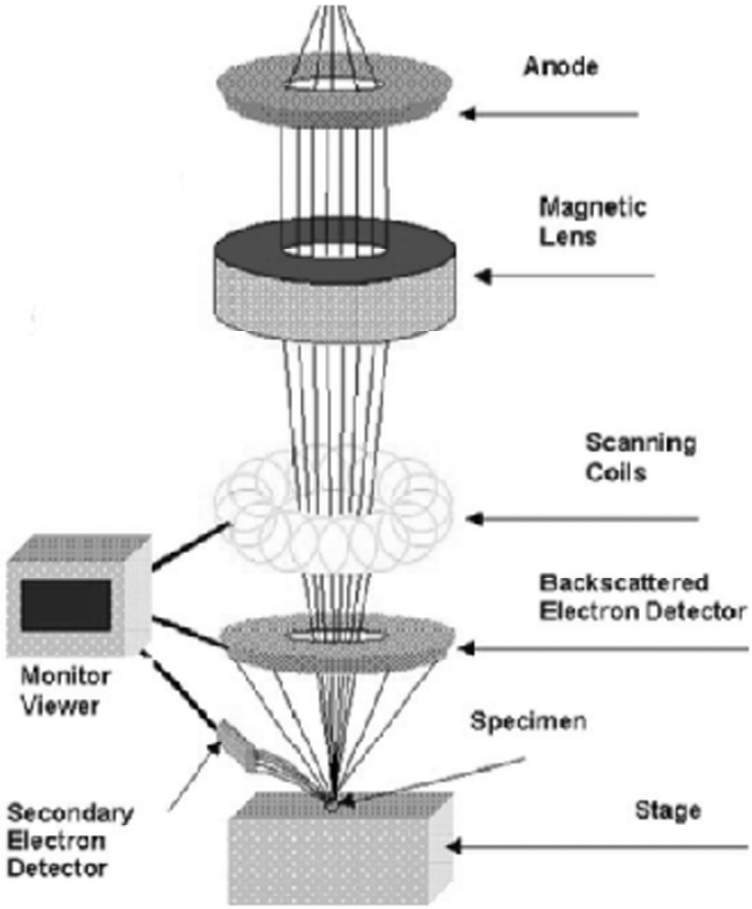


**Figure 9:** Schematic diagram of the Scanning Electron Microscope. Copyright 2013 Joseph Roy-Mayhew.

image is created, SEM images have a characteristic three-dimensional appearance and are useful for judging the surface morphology of the sample [116].

The SEM has an ability to image a comparatively large area of a specimen and also to image bulk materials. Topology of the powder samples in the present study was carried out using a FEI, Model Quanta 200 3D scanning electron microscope.

### *6.4. UV-VIS Spectroscopy*

UV-VIS Spectroscopy deals with the recording of absorption signals due to electronic transitions. In semiconductors, when the incident photon energy exceeds the band gap energy of the materials, absorption takes place and signal is recorded by the spectrometer whereas in metals when the surface free electrons vibrate coherently with the incident frequency then resonant absorption takes place. Such a spectrometer can operate in two modes (i) transmission and (ii) reflection mode. In transmission mode usually thin films and colloidal NPs well-dispersed in solvent are used. The optical measurements for opaque thin films and those NPs which are not dispersible in solvents are done in diffuse reflectance (DRS) mode [117].

Instrument: Figure 1 shows the block diagram of UV-Vis spectrophotometer. The light from the source is alternatively split into one of two beams by a chopper; one beam is passed through the sample and the other through the reference. The detector, which is often a photodiode, alternates between measuring the sample beam and the reference beam. Some double beam instruments have two detectors, and the sample and reference beam are measured at the same time. In other instruments, the two beams pass through a beam chopper which blocks one beam at a time.

### *6.5. Solar Simulator*

A solar simulator (also known as artificial sun) is a device that provides illumination approximating natural sunlight. The purpose of the solar simulator is to provide a controllable indoor test facility under laboratory conditions used for the testing of solar cells, plastics, and other materials and devices [118].

The simulator starts with a xenon arc lamp with various output powers, with the illumination area ranging from 2 × 2 inch to 8 × 8 inch. For example, a 300 W, 2 × 2 in. solar simulator can provide output densities of up to 2800 $W/m^2$, or nearly three times the typical solar irradiance level at sea level with an AM equivalent of 1.0. In Figure 14 the air-mass value AM 0 equates to isolation at sea level with the Sun at its zenith. AM 1.0 represents sunlight with the Sun at zenith above the Earth's atmosphere and absorbing oxygen and nitrogen gases. AM 1.5 is the same, but with the Sun at an oblique angle of $48.2^o$, which simulates a longer optical path through the Earth's atmosphere; AM 2.0 extends that oblique angle to $60.1^o$.

The simulator also includes a control that allows the output levels to be increased or decreased while maintaining the proper spectral ratios necessary to simulate solar irradiance. An ellipsoidal reflector collects the lamp output, and a collection mirror directs

the light through a single-blade shutter to an optical integrator that ensures uniformity variations of less than 2% across the simulator's output beam. Beam uniformity is heavily dependent on two design considerations: proper alignment of the optical elements and the optical integrator. The integrator is a monolithic optic that effectively homogenizes the collimated light to within the uniformity values listed in international photovoltaic testing standards. The light then passes through the AM spectral correction filter as shown in Figure 11. I-V measurements-such as short-circuit current (Isc), current density (Jsc), open-circuit voltage (Voc), fill factor (FF), maximum output power (Pmax) and current (Imax), voltage (Vmax), and cell efficiency (η) require a reference-cell comparison to calculate the spectral-mismatch factors for different cells and test equipment configurations [119]. A Newport Silicon Reference Cell is used as reference cell for optimization of solar simulator. The reference cell is connected to readout electronics that displays measured solar simulator irradiance and cell temperature. These values are entered as parameters in the I-V measurement software and are used to generate accurate and repeatable I-V performance. Proper integration between software, solar simulator, and reference cell is necessary to achieve accurate, repeatable data to calculate the solar cell efficiency. Once the solar simulator and other instruments are turned on and the cell is placed beneath the simulator, the software will open the solar-simulator shutter, sweep the voltage across the prescribed range, measure the current, and display the I-V curve. Then the software calculates the key solar cell parameters discussed previously, including the cell conversion efficiency.

### *6.6. Incident photon-to-current conversion efficiency (IPCE) Measurements*

Another fundamental measurement of the performance of a solar cell is the "external quantum efficiency", which in the DSSC community is normally called the incident photon to current conversion efficiency (IPCE) [120]. The IPCE value corresponds to the photocurrent density produced in the external circuit under monochromatic illumination of the cell divided by the photon flux that strikes the cell.

## 7. Graphene Application in other type of solar cell

For many of the same reasons that they have been used in DSSCs, graphene materials have also been used in other types of solar cells. A brief overview is included here to

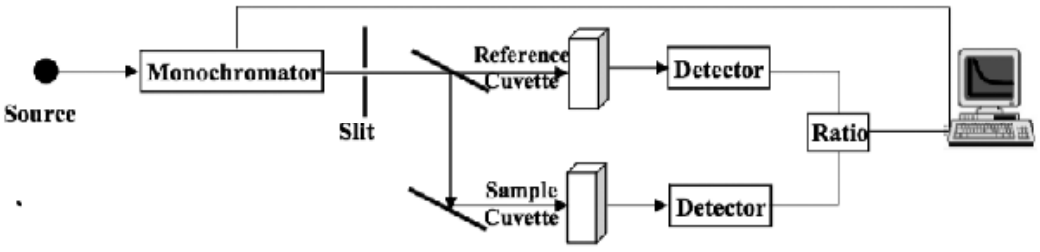


**Figure 10:** Schematics of UV-VIS Spectrophotometer in Transmission Mode. Copyright 2013 Joseph Roy-Mayhew.

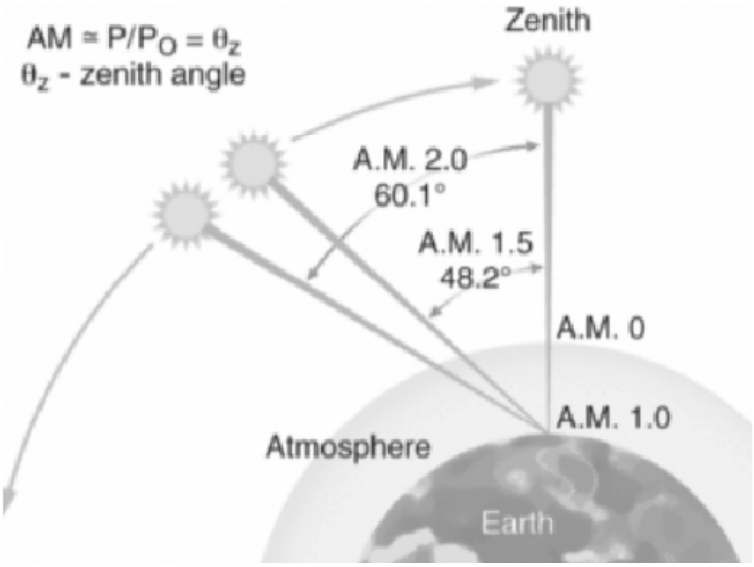


**Figure 11:** Air-Mass calculations for 1 Sun measurements. Copyright 2011 American Chemical Society.

provide context for the DSSC work. As mentioned, transparent conductors are a large potential market, and having cost-effective TCFs would allow improvements to conventional silicon solar cell technologies as well as to the thin film technologies (cadmium telluride, copper indium gallium selenide, organic, etc.), allowing for device structure modification, and a reduction in the number of silver contact lines on devices. Along these lines, a graphene material-based conductive ink could displace silver current collectors in the gamut of solar cell technologies. Currently, it is estimated that silver contact lines represent about $0.04/WP of devices and is highly dependent on the cost of silver. Furthermore, most silver pastes currently marketed have to be sintered at elevated temperatures (>400 °C), increasing processing costs and limiting substrate selection [121]. To be applicable, any replacement inks would have to achieve similar conductivity, both along the busbars and in contacting the device TCF without shading more of the device, a daunting task. In organic solar cells, graphene materials have been used as electron acceptors and hole conductors, which a few reviews summarize. Additionally, graphene materials have been used to form Schottky junctions with $CdSe_2$ and $Si_2$ with the later device achieving $\eta > 8\%$. In line with this work, researchers have used graphene dispersions to facilitate stable growth of attached nanoparticles for quantum dot solar cells and for solar fuel applications. Lastly, fundamental studies of graphene have shown hot carrier transport and multiple carrier generation from a single photon, both effects which overcome the limits imposed on devices based on the band gap of semiconductors, and thus, a graphene photovoltaic device could obtain very high efficiencies in the future. Graphene materials have been used with a range of solar cell technologies, but what is distinguishing about DSSCs is that graphene materials, with their wide range of properties, have been used in almost all aspects of the device.

## 8. Conclusions and outlook

Although graphene materials can be used to improve DSSCs in a variety of roles, particular functions are best performed by specific graphene materials. Pristine graphene, followed by highly reduced graphene oxide, have the best prospects for transparent conductors, though by themselves the materials are not sufficient to meet application demands. These materials will have to either be electronically doped or exist as a part of a metal hybrid system. In the photoanode, graphene materials have resulted in improved photocurrent; however, it is unclear whether the advantages will apply to optimized devices. Whether graphene oxide, CRGO, or TRGO is processed with the $TiO_2$ is unlikely to mater significantly, as heat treatment is generally required to sinter the $TiO_2$ layer, which will thermally reduce the graphene material. If there is a percolated graphene material network then sintering may not be necessary; however, each $TiO_2$ particle would have to be in contact with the graphene material network for best results. In this case, the sheets would have to be conducting and well dispersed through the $TiO_2$ matrix, so starting processing with graphene oxide and then reducing the material is a promising option. Pristine graphene could be advantageous in this application due to its high conductivity and relative inertness, but processing would be difficult, limiting application. Graphene materials can be used as a sensitizer in solar cells, and quantum effects, in particular, hot injection, could allow cells to exceed the Shockley"Queisser efficiency limit. Nevertheless, optimization processing of graphene quantum dots has brought the material closer to current organic dye structures. Graphene oxide could be a useful gelling agent in the electrolyte, whereas RGO in this role will likely catalyze recombination and reduce cell efficiency. At the cathode, two approaches have been shown that can equal or surpass the performance of platinum nanoparticles: (i) high surface area electrodes and (ii) high-activity materials. In both approaches RGO is advantageous as pristine graphene is relatively inert. In the first case, care must be taken to prevent restacking of sheets, while in the second, either a highly active nanoparticle composite can be formed or a redox mediator for which reduced graphene oxide is highly active (e.g., Co- $(bpy)_3$(II/III)) can be used. Use of graphene materials in DSSCs has seen a rapid increase in research and fruitful results. Nevertheless, as research progresses, it is important to keep in mind that the various graphene materials have different properties integrally tied to their method of production and each may be beneficial to different areas in a solar cell. A next stage of research, to bring graphene materials to higher relevance in the DSSC community, would be to study whether improvements discussed within this review can be carried over to the current best-in-class devices.

### *Notes and References*

[1] Energy Technology Perspectives 2015, International Energy Agency, Paris, France (2015), *http://www.iea.org/etp*.

[2] C. Philibert, Solar energy perspectives 2011, Organisation for Eco- nomic Co-operation and Development and International Energy Agency, Paris, France (2011).

[3] International Technology Roadmap for Photovoltaic (ITRPV). *http://www.itrpv.net.*

[4] T. Bradford, Solar Revolution: The Economic Transformation of the Global Energy Industry, MIT Press, Cambridge (2006).

[5] V. Balzani and N. Armaroli, Energy for a Sustainable World— From the Oil Age to a Sun-Powered Future, Wiley-VCH, Weinheim (2011).

[6] R. A. Ristinen and J. J. Kraushaar, Energy and the Environment, John Wiley & Sons, New York (2006).

[7] J. K. Rath, Low temperature polycrystalline silicon: A review on deposition, physical properties and solar cell applications. Solar Energy Mater. Solar Cells 76, 431–487 (2003).

[8] A. V. Shah, H. Schade, M. Vanecek, J. Meier, E. Vallat-Sauvain, N. Wyrsch, U. Kroll, C. Droz, and J. Bailat, Thin-film silicon solar cell technology. Prog. Photovolt. Res. Appl. 12, 113–142 (2004).

[9] X. Liu, P. R. Coxon, M. Peters, B. Hoex, J. M. Cole, and D. J. Fray, Black silicon: Fabrication methods, properties and solar energy applications. Energy Environ. Sci. 7, 3223–3263 (2014).

[10] W. H. Bloss, F. Pfisterer, M. Schubert, and T. Walter, Thin-film solar cells. Prog. Photovolt: Res. Appl. 3, 3–24 (1995).

[11] A. Shah, P. Torres, R. Tscharner, N. Wyrsch, and H. Keppner, Pho- tovoltaic technology: The case for thin-film solar cells. Science 285, 692–698 (1999).

[12] K. L. Chopra, P. D. Paulson, and V. Dutta, Thin-film solar cells: An overview. Prog. Photovolt: Res. Appl. 12, 69–92 (2004).

[13] P. V. Kamat, Quantum dot solar cells: Semiconductor nanocrystals as light harvesters. J. Phys. Chem. C 112, 18737–18753 (2008).

[14] S. Ruhle, M. Shalom, and A. Zaban, Quantum-dot-sensitized solar cells. ChemPhysChem. 11, 2290–2304 (2010).

[15] K. M. Coakley and M. D. McGehee, Conjugated polymer photo- voltaic cells. Chem. Mater. 16, 4533–4542 (2004).

[16] Y.-J. Cheng, S.-H. Yang, and C.-S. Hsu, Synthesis of conju- gated polymers for organic solar cell applications. Chem. Rev. 109, 5868–5923 (2009).

[17] (a) N. J. Jeon, J. H. Noh, W. S. Yang, Y. C. Kim, S. Ryu, J. Seo, and S. I. Seok, Compositional engineering of perovskite materi- als for high-performance solar cells. Nature517, 476–480 (2015).

[18] (a) T. E. Graedel, E. M. Harper, N. T. Nassar, P. Nuss, and B. K. Reck, Criticality of metals and metalloids. Proc. Nat. Acad. Sci. USA 201500415 (2015).

[19] Minerals, Critical Minerals, and the U.S. Economy, National Research Council, National Academies Press, Washington D.C. (2008); National Research Council (US) Chemical Sciences Roundtable, Assessments of Criticality (2012).

[20] E. Singh and H. S. Nalwa, Graphene-based bulk-heterojunction solar cells: A review. J. Nanosci. Nanotechnol. 15, 6237–6278 (2015).

[21] R. R. Nair, P. Blake, A. N. Grigorenko, K. S. Novoselov, T. J. Booth, T. Stauber, N. M. R. Peres, and A. K. Geim, Fine struc- ture constant defines visual transparency of graphene. Science 320, 1308–1308 (2008).

[22] (a) X. Li, Y. Zhu, W. Cai, M. Borysiak, B. Han, D. Chen, R. D. Piner, L. Colombo, and R. S. Ruoff, Transfer of large-area graphene films for high-performance transparent conductive electrodes. Nano Lett. 9, 4359–4363 (2009).

[23] C. Lee, X. Wei, J. W. Kysar, and J. Hone, Measurement of the elas- tic properties and intrinsic strength of monolayer graphene. Science 321, 385–388 (2008).

[24] L. Zhang, J. Liang, Y. Huang, Y. Ma, Y. Wang, and Y. Chen, Size- controlled synthesis of graphene oxide sheets on a large scale using chemical exfoliation. Carbon 47, 3365–3380 (2009).

[25] J. Shen, Y. Hu, C. Li, C. Qin, M. Shi, and M. Ye, Layer-by-layer self-assembly of graphene nanoplatelets. Langmuir 25, 6122–6128 (2009).

[26] P. W. Sutter, J. I. Flege, and E. A. Sutter, Large-scale pattern growth of graphene films for stretchable transparent electrodes. Nature Mater. 7, 406–411 (2008).

[27] G. Eda, G. Fanchini, and M. Chhowalla, Large-area ultrathin films of reduced graphene oxide as a transparent and flexible electronic material. Nature Nanotechnol. 3, 270–274 (2008).

[28] K. S. Kim, Y. Zhao, H. Jang, S. Y. Lee, J. M. Kim, K. S. Kim, J.-H. Ahn, P. Kim, J.-Y. Choi, and B. H. Hong, Large-scale pat- tern growth of graphene films for stretchable transparent electrodes. Nature 457, 706–710 (2009).

[29] Y.-W. Son, M. L. Cohen, and S. G. Louie, Half-metallic graphene nanoribbons. Nature 444, 347–349 (2006).

[30] M. Y. Han, B. Ozyilmaz, Y. B. Zhang, and P. Kim, Energy band-gap engineering of graphene nanoribbons. Phys. Rev. Lett. 98, 206805 (2007).

[31] X. Li, X. Wang, L. Zhang, S. Lee, and H. Dai, Chemically derived, ultrasmooth graphene nanoribbon semiconductors. Science 319, 1229–1232 (2008).

[32] F. Yavari, Z. Chen, A. V. Thomas, W. Ren, H.-M. Cheng, and N. Koratkar, High sensitivity gas detection using a macroscopic three-dimensional graphene foam network. Sci. Rep. 1 (2011), Article number 166, doi:10.1038/srep00166.

[33] Z. Chen, C. Xu, C. Ma, W. Ren and H.-M. Cheng, Lightweight and flexible graphene foam composites for high-performance electro- magnetic interference shielding. Adv. Mater. 25, 1296–1300 (2013).

[34] D. W. Zhang, X. D. Li, H. B. Li, S. Chen, Z. Sun, X. J. Yin, and S. M. Huang, Graphene-based counter electrode for dye-sensitized solar cells. Carbon 49, 5382–5388 (2011).

[35] H.-S. Jang, J.-M. Yun, D.-Y. Kim, D.-W. Park, S.-I. Na, and S.-S. Kim, Moderately reduced graphene oxide as transparent counter electrodes for dye-sensitized solar cells. Electrochim. Acta 81, 301–307 (2012).

[36] H. Chen, M. B. Muller, K. J. Gilmore, G. G. Wallace, and D. Li, Mechanically Strong, Electrically conductive, and biocompatible graphene paper. Adv. Mater. 20, 3557–3561 (2008).

[37] J. C. Meyer, A. K. Geim, M. I. Katsnelson, K. S. Novoselov, T. J. Booth, and S. Roth, The structure of suspended graphene sheets. Nature 446, 60–63 (2007).

[38] J. Velten, A. J Mozer, D. Li, D. Officer, G. Wallace, R. Baughman, and A. Zakhidov, Carbon nanotube/ graphene nanocomposite as efficient counter electrodes in dye-sensitized solar cells. Nanotechnology 23, 085201 (2012).

[39] Z. Yang, M. Liu, C. Zhang, W. W. Tjiu, T. Liu, and H. Peng, Carbon nanotubes bridged with graphene nanoribbons and their use in high-efficiency dye-sensitized solar cells. Angew. Chem. Int. Ed. 52, 3996–3999 (2013).

[40] J. Ma, L. Zhou, C. Li, J. Yang, T. Meng, H. Zhou, M. Yang, F. Yu, and J. Chen, Surfactant-free synthesis of graphene-functionalized carbon nanotube film as a catalytic counter electrode in dye- sensitized solar cells. J. Power Sources 247, 999–1004 (2014).

[41] H. Zheng, C. Y. Neo, and J. Ouyang, Highly efficient iodide/triiodide dye-sensitized solar cells with gel-coated reduce graphene oxide/single-walled carbon nanotube composites as the counter electrode exhibiting an open-circuit voltage of 0.90 V. ACS Appl. Mater. Interfaces 5, 6657–6664 (2013).

[42] D. C. Elias, R. R. Nair, T. M. G. Mohiuddin, S. V. Morozov, P. Blake, M. P. Halsall, A. C. Ferrari, D. W. Boukhvalov, M. I. Katsnelson, A. K. Geim, and K. S. Novoselov. Control of Graphene's Properties by Reversible Hydrogenation: Evidence for Graphane. Science 323, 610–613 (2009).

[43] R. Balog, B. Jorgensen, L. Nilsson, M. Andersen, E. Rienks, M. Bianchi, M. Fanetti, E. Laegsgaard, A. Baraldi, S. Lizzit, Z. Sljivancanin, F. Besenbacher, B. Hammer, T. G. Pedersen, P. Hofmann, and L. Hornekaer, Bandgap opening in graphene induced by patterned hydrogen adsorption. Nature Mater. 9, 315–319 (2010).

[44] M. Pumera and C. H. A. Wong, Graphene and hydrogenated graphene. Chem. Soc. Rev. 42, 5987–5995 (2013).

[45] R. Jayasingha, A. Sherehiy, S. Y. Wu, and G. U. Sumanasekera, In situ study of hydrogenation of graphene and new phases of localization between metal–insulator transitions. Nano Lett. 13, 5098–5105 (2013).

[46] A. H. C. Neto and K. Novoselov, 2D crystals: Beyond graphene. Mater. Express 1, 10–17 (2011).

[47] Y. Zhang, Y.-W. Tan, H. L. Stormer, and P. Kim, Experimen- tal observation of the quantum Hall effect and Berry's phase in graphene. Nature 438, 201–204 (2005).

[48] R. Saito, M. Fujita, G. Dresselhaus, and M. S. Dresselhaus, Electronic structure of chiral graphene tubules. Appl. Phys. Lett. 60, 2204–2206 (1992).

[49] A. A. Balandin, Thermal properties of graphene and nanostructured carbon materials. Nature Mater. 10, 569–581 (2011).

[50] M. Meyyappan (ed)., Carbon Nanotubes: Science and Applications, CRC Press, Boca Raton, FL (2004).

[51] W. U. Huynh, J. J. Dittmer, and A. P. Alivisatos, Hybrid nanorod- polymer solar cells. Science 295, 2425–2427 (2002).

[52] M. D. McGehee, Nanostructured organic–inorganic hybrid solar cells. Mater. Res. Soc. Bull. 34, 95–100 (2009).

[53] B. C. Thompson and J. M. J. Frechet, Polymer–fullerene composite solar cells. Angew. Chem. Int. Ed. 47, 58–77 (2008).

[54] G. Dennler, M. C. Scharber, and C. J. Brabec, Polymer–fullerene bulk heterojunction solar cells. Adv. Mater. 21, 1323–1338 (2009). 55. A. I. Hochbaum and P. Yang, Semiconductor nanowires for energy conversion. Chem. Rev. 110, 527–546 (2010).

[55] W. Sun, T. Peng, Y. Liu, S. Xu, J. Yuan, S. Guo, and X.-Z. Zhao, Hierarchically porous hybrids of polyaniline nanoparticles anchored on reduced graphene oxide sheets as counter electrodes, for dye-sensitized solar cells. J. Mater. Chem. A 1, 2762–2768 (2013).

[56] E. C. Garnett, M. L. Brongersma, Y. Cui, and M. D. McGehee, Nanowire solar cells. Annu. Rev. Mater. Res. 41, 269–295 (2011). 57. C. J. Brabec, S. Gowrisanker, J. J. Halls, D. Laird, S. Jia, and S. P. Williams, Polymer–fullerene bulk-heterojunction solar cells. Adv. Mater. 22, 3839–3856 (2010).

[57] K. S. Lee, Y. Lee, J. Y. Lee, J.-H. Ahn, and J. H. Park, Flexible and platinum free dye-sensitized solar cells with conducting polymer- coated graphene counter electrodes. ChemSusChem 5, 379–382 (2012).

[58] H. S. Nalwa (ed.), Handbook of Nanostructured Materials and Nanotechnology, Academic Press, San Diego, CA (2000), Vols. 1–5.

[59] H. S. Nalwa (ed.), Encyclopedia of Nanoscience and Nano-technology, American Scientific Publishers, Los Angeles, CA (2004/2011), Vols. 1–25.

[60] H. S. Nalwa (ed.), Handbook of Advanced Electronic and Photonic Materials and Devices, Academic Press, San Diego, CA (2001), Vols. 1–10.

[61] H. S. Nalwa and L. S. Rohwer (eds.), Handbook of Luminescence, Display Materials and Devices, American Scientific Publish-ers, Los Angeles, CA (2003), Vols. 1–3.

[65] H. S. Nalwa (ed.), Handbook of Nanostructured Biomaterials and Their Applications in Nanobiotechnology, American Scientific Publishers, Los Angeles, CA (2005), Vols. 1–2.

[66] H. S. Nalwa and T. J. Webster (eds.), Cancer Nanotechnology Nanomaterials for Cancer Diagnosis and Therapy, American Scientific Publishers, Los Angeles, CA (2008).

[67] S. Singh, Nanomedicine-nanoscale drugs and delivery systems. J. Nanosci. Nanotechnol. 10, 7906–7918 (2010).

[68] R. Singh and H. S. Nalwa, Medical applications of nanoparticles in biological imaging, cell labeling, antimicrobial agents, and anti-cancer nanodrugs. J. Biomed. Nanotechnol. 7, 489–503 (2011).

[69] H. S. Nalwa, A special issue on reviews in nanomedicine, drug delivery and vaccine development. J. Biomed. Nanotechnol.10, 1635–1640 (2014).

[70] H. S. Nalwa, A special issue on reviews in biomedical applications of nanomaterials, tissue engineering, stem cells, bioimaging, and toxicity. J. Biomed. Nanotechnol. 10, 2421–2423 (2014).

[71] W. F. Schmidt and S. Singh, The nano man from India: In cele- bration of the 60th birthday of Dr. Hari Singh Nalwa. J. Nanosci. Nanotechnol. 14, 1–14 (2014).

[72] T. Soga (ed)., Nanostructured Materials for Solar Energy Conversion, Elsevier, Amsterdam (2006).

[73] X. Chen and S. S. Mao, Titanium dioxide nanomaterials: Synthesis, properties, modifications, and applications. Chem. Rev. 107, 2891–2959 (2007).

[74] M. Toivola, J. Halme, K. Miettunen, K. Aitola, and P. D. Lund, Nanostructured dye solar cells on flexible substrates—Review.Int. J. Energy Res. 33, 1145–1160 (2009).

[75] H. S. Nalwa (ed.), Nanomaterials for Energy Storage Applications, American Scientific Publishers, Los Angeles, CA (2009).

[76] Q. Zhang, E. Uchaker, S. L. Candelaria, and G. Cao, Nanomaterials for energy conversion and storage. Chem. Soc. Rev. 42, 3127–3171 (2013).

[77] C. Berger, Z. Song, T. Li, X. Li, A. Y. Ogbazghi, R. Feng, Z. Dai, A. N. Marchenkov, E. H. Conrad, P. N. First, and W. A. de Heer, Ultrathin epitaxial graphite: 2D electron gas properties and a route toward graphene-based nanoelectronics. J. Phys. Chem. B 108, 19912 (2004).

[78] S. Latil and L. Henrard, Charge carriers in few-layer graphene films. Phys. Rev. Lett. 97, 036803–6 (2006).

[79] T. Mueller, F. N. Xia, and P. Avouris, Graphene photodetectors for high-speed optical communications. Nature Photon. 4, 297–301 (2010).

[80] Y.-M. Lin, C. Dimitrakopoulos, K. A. Jenkins, D. B. Farmer, H.-Y. Chiu, A. Grill, and P. Avouris, 100 GHz transistors from wafer scale epitaxial graphene. Science 327, 662 (2010).

[81] D. Lee, K. Lee, K. Kim, and O. Kim, New analytical drain current model for the sub-linear region of output characteristics of graphene field-effect transistors in the low carrier density limit. J. Nanosci. Nanotechnol. 14, 9082–9087 (2014).

[82] F. Rana, Graphene terahertz plasmon oscillators. IEEE Trans. Nanotechnol. 7, 91–99 (2008).

[83] F. N. Xia, T. Mueller, Y. M. Lin, A. Valdes-Garcia, and P. Avouris, Ultrafast graphene photodetector. Nature Nanotechnol. 4, 839–843 (2009).

[84] M. D. Stoller, S. Park, Y. W. Zhu, J. H. An, and R. S. Ruoff, Graphene-based ultracapacitors. Nano Lett. 8, 3498–3502 (2008).

[87] F. Schedin, A. K. Geim, S. V. Morozov, E. W. Hill, P. Blake, M. I. Katsnelson, and K. S. Novoselov, Detection of individual gas molecules adsorbed on graphene. Nature Mater. 6, 652–655 (2007).

[88] H. Shen, L. Zhang, M. Liu, and Z. Zhang, Biomedical applications of graphene. Theranostics 2, 283–294 (2012).

[89] L. Z. FengandZ. Liu,Graphene in biomedicine: Opportunities and challenges. Nanomedicine 6, 317–324 (2011).

[90] L. Z. Feng, S. Zhang, and Z. Liu, Graphene based genetransfection.Nanoscale 3, 1252–1257 (2011).

[91] A. Lerf, H. Y. He, M. Forster, and J. Klinowski, Structure of graphite oxide revisited. J. Phys. Chem. B 102, 4477–4482 (1998).

[92] H. He, J. Klinowski, M. Forster, and A. Lerf, A new structural model for graphite oxide. Chem. Phys. Lett. 287, 53–56 (1998).

[93] W. Gao, L. B. Alemany, L. Ci, and P. M. Ajayan, New insights into the structure and reduction of graphite oxide. Nature Chem.1, 403–408 (2009).

[94] C. Hontoria-Lucas, A. J. Lopez-Peinado, J. D. Lopez-Gonzalez, M. L. Rojas-Cervantes, and R. M. Martin-Aranda, Study of oxygen- containing groups in a series of graphite oxides: Physical and chem- ical characterization. Carbon 33, 1585–1592 (1995).

[95] T. Szabo, O. Berkesi, and I. Dekany, DRIFT study of deuterium- exchanged graphite oxide. Carbon 43, 3186–3189 (2005).

[96] C. Mattevi, G. Eda, S. Agnoli, S. Miller, K. A. Mkhoyan, O. Celik, D. Mastrogiovanni, G. Granozzi, E. Garfunkel, and M. Chhowalla, Evolution of electrical, chemical, and structural properties of trans- parent and conducting chemically derived graphene thin films. Adv. Funct. Mater. 19, 2577–2583 (2009).

[97] H. C. Schniepp, J.-L. Li, M. J. McAllister, H. Sai, M. Herrera- Alonso, D. H. Adamson, R. K. Prud'homme, R. Car, D. A. Saville, and I. A. Aksay, Functionalized single graphene sheets derived from splitting graphite oxide. J. Phys. Chem. B 110, 8535–8539 (2006).

[98] S. Stankovich, D. A. Dikin, R. D. Piner, K. A. Kohlhaas, A. Kleinhammes, Y. Jia, Y. Wu, S. T. Nguyen, and R. S. Ruoff, Synthesis of graphene-based nanosheets via chemical reduction of exfoliated graphite oxide. Carbon 45, 1558–1565 (2007).

[99] (a) D. R. Dreyer, S. Park, C. W. Bielawski, and R. S. Ruoff, The chemistry of graphene oxide. Chem. Soc. Rev. 39, 228–240 (2009); (b) S. Park and R. S. Ruoff, Chemical methods for the production of graphenes. Nature Nanotechnol. 4, 217–224 (2009).

[100] A.Mathkar,D.Tozier,P.Cox,P.Ong,C.Galande,K.Balakrishnan, A. L. M. Reddy, and P. M. Ajayan, Controlled, stepwise reduction and band gap manipulation of graphene oxide. J. Phys. Chem. Lett. 3, 986–991 (2012).

[101] (a) B. O'Regan and M. Gratzel, A low-cost, high-efficiency solar cell based on dye-sensitized colloidal TiO2 films. Nature 353, 737–740 (1991);

[102] M. K. Nazeeruddin, P. Pechy, and M. Gratzel, Efficient panchro- matic sensitization of nanocrystalline TiO2 films by a black dye based on a trithiocyanato-ruthenium complex. Chem. Commun. 1705–1706 (1997).

[103] M. K. Nazeeruddin, P. Pechy, T. Renouard, S. M. Zakeeruddin, R. Humphry-Baker, P. Comte, P. Liska, L. Cevey, E. Costa, V. Shklover, L. Spiccia, G. B. Deacon, C. A. Bignozzi, and M. Gratzel, Engineering of efficient panchromatic sensitizers for nanocrystalline TiO2-based solar cells. J. Am. Chem. Soc. 123 1613–1624 (2001).

[104] G. K. Mor, O. K. Varghese, M. Paulose, K. Shankar, and C. A. Grimes, A review on highly ordered, vertically oriented TiO2 nano- tube arrays: Fabrication, material properties, and solar energy applications. Solar Energy Materials and Solar Cells 90, 2011–2075 (2006).

[105] F. O. Lenzmann and J. M. Kroon, Recent advances in dye- sensitized solar cells. Adv. OptoElectron. 65073/1–65073/10 (2007).

[106] B. E. Hardin, H. J. Snaith, and M. D. McGehee, Renaissance of dye-sensitized solar cells. Nature Photonics 6, 162–169 (2012).

[107] A. Hagfeldt and M. Graetzel, Light-induced redox reactions in nanocrystalline systems. Chem. Rev. 95, 49–68 (1995).

[108] A. Hagfeldt and M. Gratzel, Molecular photovoltaics. Acc. Chem. Res. 33, 269–277 (2000).

[109] G. Boschloo and A. Hagfeldt, Characteristics of the iodide/triiodide redox mediator in dye-sensitized solar cells. Acc. Chem. Res. 42, 1819–1826 (2009).

[110] A.Hagfeldt,G.Boschloo,L.Sun,L.Kloo,andH.Pettersson,Dye- sensitized solar cells. Chem. Rev. 110, 6595–6663 (2010).

[111] Q. Zhang and G. Cao, Nanostructured photoelectrodes for dye- sensitized solar cells. Nano Today 6, 91–109 (2011).

[112] L. Mao and J. Chen, Arylamine organic dyes for dye-sensitized solar cells. Chem. Soc. Rev. 42, 3453–3488 (2013).

[113] B. Li, L. Wang, B. Kang, P. Wang, and Y. Qiu, Review of recent progress in solid-state dye-sensitized solar cells. Solar Energy Materials and Solar Cells 90, 549–573 (2006).

[114] Y. S. Yen, H.-H. Chou, Y.-C. Chen, C.-Y. Hsu, and J. T. Lin, Recent developments in molecule-based organic materials for dye- sensitized solar cells. J. Mater. Chem. 22, 8734–8747 (2012).

[115] S. Wenger, S. Seyrling, A. N. Tiwari, and M. Gratzel, Appl. Phys. Lett. 94, 173508 (2009).

[116] F. Hao, P. Dong, Q. Luo, J. Li, J. Lou, and H. Lin, Recent advances in alternative cathode materials for iodine-free dye-sensitized solar cells. Energy Environ. Sci. 6, 2003–2019 (2013).

[117] S. Thomas, T. G. Deepak, G. S. Anjusree, T. A. Arun, S. V. Nair, and A. S. Nair, A review on counter electrode materials in dye- sensitized solar cells. J. Mater. Chem. A 2, 4474–4490 (2014).

[118] M. Wu and T. Ma, Recent progress of counter electrode catalysts in dye-sensitized solar cells. J. Phys. Chem. C 118, 16727–16742 (2014).

[119] U. Bach, D. Lupo, P. Comte, J. E. Moser, F. Weissortel, J. Salbeck, H. Spreitzer, and M. Gratzel, Solid-state dye-sensitized mesoporous $TiO_2$ solar cells with high photon-to-electron conversion efficiencies. Nature 395, 583–585 (1998).

[120] J. Mac'aira, L. Andrade, and A. Mendes, Review on nanostruc- tured photoelectrodes for next generation dye-sensitized solar cells. Renewable and Sustainable Energy Reviews 27, 334–349 (2013).

[121] M. Ye, X. Wen, M. Wang, J. Iocozzia, N. Zhang, C. Lin, and Z. Lin, Recent advances in dye-sensitized solar cells: From pho- toanodes, sensitizers and electrolytes to counter electrodes. Mater. Today 18, 155–162 (2015).